Intrinsic Opening of BK Channels Derives from Inherent Leakage in Hydrophobic Gating

Zhiguang Jia[1,#], Guohui Zhang[2,#], Jingyi Shi[2], Jianmin Cui[2,*], and Jianhan Chen[1,*]

[1]Department of Chemistry, University of Massachusetts, Amherst, MA 01003, USA

[2]Department of Biomedical Engineering, Center for the Investigation of Membrane Excitability Disorders, Cardiac Bioelectricity and Arrhythmia Center, Washington University, St Louis, MO 63130, USA

* Corresponding Authors: jcui@wustl.edu (Cui), jianhanc@umass.edu (Chen)

# Equal contributions

Abstract

The big potassium (BK) channels remain open with a small limiting probability of $P_o \sim 10^{-7}$ at minimal Ca^{2+} and negative voltages < -100 mV. The molecular origin and functional significance of such “intrinsic opening” are not understood. Here we combine atomistic simulations and electrophysiological experiments to show that the intrinsic opening of BK channels is an inherent property of the vapor barrier, generated by hydrophobic dewetting of the BK inner pore in the deactivated state. The vapor barrier only gives rise to a finite free energy barrier, of ~ 8 kcal/mol, and cannot completely shut down K^+ flow even when the voltage sensor domains are fully deactivated. This results in the leaking currents that can be measured at negative voltages as the indication of intrinsic opening. The shallow limiting slope of P_o at negative voltages results primarily from the electric field effects on the permeating ion through the vapor barrier. We further demonstrate that the vapor barrier can be perturbed by inner pore mutations and truncation of the cytosolic domains, leading to predicable changes in limiting slope measurements. Therefore, the intrinsic opening in BK channels, and possibly in other ion channels, opens up an opportunity to experimentally study hydrophobic gating. Our results further suggest that intrinsic opening in BK channels is the fundamental basis for the allosteric mechanism of activation by both voltage and Ca^{2+}.

Introduction

Large conductance Ca2+-activated K^+ (BK) channels, also known as KCa1.1 or SLO1 channels, exhibit the highest single-channel conductance of 100-300 pS among all K^+ channels (1-5). Formed by four Slo1 subunits, functional BK channels can be activated independently and synergistically in response to membrane depolarization, through the voltage sensing domains (VSDs), and binding of intracellular Ca^{2+} and Mg^{2+} , through the C-terminal domains (CTDs) (Fig. 1a) (6-9). By linking intracellular Ca^{2+} signal to cell excitability, BK channels play a central role in many important physiological processes (10, 11), and are implicated in many cardiovascular and neurological diseases (12). BK channels are considered promising therapeutic targets for multiple diseases including epilepsy (13), lysosomal storage diseases (14), temporal lobe seizures (15), hypertension (16) and dyskinesia (17). There is a great need to further understand the gating and regulatory mechanisms of BK channels at the molecular level.

BK channels differ significantly from canonical voltage-gated K^+ (Kv) channels in both the tetrameric topology and pore conformations. The voltage sensor domains (VSDs) are domain-swapped with respect to the pore-gate domain (PGD) in Kv channels (18-21). In contrast, cryo-EM structures of the whole-length BK channels reveal that VSDs and PGDs are not domain-swapped (22-27), which is a key feature that likely underlies distinct voltage gating characteristics and mechanisms (28). Another important difference is that a classical Kv channel is closed by pinching the domain-swapped pore lining helices at the intracellular entrance, creating a bundle crossing gate that physically obstructs K^+ entrance from the cytoplasmic side (3, 29-31). However, bundle crossing is absent in all available cryo-EM structures of BK channel (22-27), and the pore of BK channels remain physically open with a diameter of ~10 Å even in the Ca^{2+}-free, deactivated state. Molecular dynamics (MD) simulations suggested that BK channels likely followed the hydrophobic gating mechanism (32-34). Here, changes in the shape and surface hydrophobicity of the inner pore in the Ca^{2+}-free state allow it to undergo spontaneous hydrophobic dewetting, giving rise to a (water) vapor barrier to block the ion flow. The dry pore remains physically open and accessible to quaternary ammonium channel blockers (32), which has been observed experimentally but not understood previously (35, 36). The hydrophobic gating mechanism also readily explains methanethiosulfonate reagent accessibility experiments (37), as well as systematic scanning mutagenesis studies and free energy calculations showing that modulation of pore hydrophobicity is strongly correlated with BK channel activation (34, 38).

Hydrophobic gating has now been recognized for dozens of channels, which are activated by voltage, mechanical force, and/or ligand binding and include both domain-swapping and non-

domain-swapping channels (39, 40). It has been proposed that hydrophobic gating could work synergistically with bundle crossing in channels where both features co-exist (41). Yet, the experimental support for hydrophobic gating in ion channels has been indirect and largely based on structural, mutagenesis and computational analysis. No effective experimental assay has been developed to directly validate and further explore this noncanonical gating mechanism. The key difficulty is the lack of effective assays to functionally study the gate in the closed state, when dewetting has happened and the vapor plug is formed. Curiously, it is well known that BK channels have a small but measurable "intrinsic opening" at very negative voltages (<-100 mV) and minimal intracellular Ca^{2+} (6, 42-44). As shown in Fig. 1b, the open probability (P_o) at these voltages is weakly voltage dependent (red slope), distinct from canonical Kv channels where P_o continues to decrease exponentially as a function of voltage (blue slope) (45, 46). We observe that a vapor barrier will only give rise to a finite free energy barrier to ion permeation (32). Thus, it cannot completely shut down ionic current even if the channel is completely driven into the deactivated conformational state (such as under 0 mM Ca^{2+} and large negative voltages). That is, unlike physical blockage formed by bundle crossing, hydrophobic gating channels are inherently leaky, and the intrinsic opening of BK channels may originate from the leakage property of the vapor barrier under deactivated conditions.

In this work, we integrate atomistic simulations, mutagenesis, and electrophysiology to test the hypothesis that intrinsic opening of BK channels derives from leakage in hydrophobic gating. We show that the free energy profiles of ion permeation of the vapor barrier quantitatively predict intrinsic opening probabilities. Free energy analysis further suggests that the shallow voltage dependence of P_o is primarily due to the electric field effects on the permeating ion through the vapor barrier. In addition, we explore two orthogonal approaches to perturb the vapor barrier, via truncation of the entire cytosolic gating ring and mutations of pore-lining residues. Combined simulation and experiments show that these perturbations of the vapor barrier lead to predictable and measurable changes in intrinsic opening. Taken together, our results strongly support the notion that intrinsic opening is an inherent property of hydrophobic gating. Furthermore, intrinsic opening allows direct study of the hydrophobic gate, using well-developed limiting slope (47) to measure the leaking current when the vapor barrier is formed. It provides a straightforward and label-less assay to dissect how the structure, shape and surface properties of the inner pore as well as binding of Ca^{2+} and other ligands may control the vapor barrier in BK and other hydrophobic gating channels.

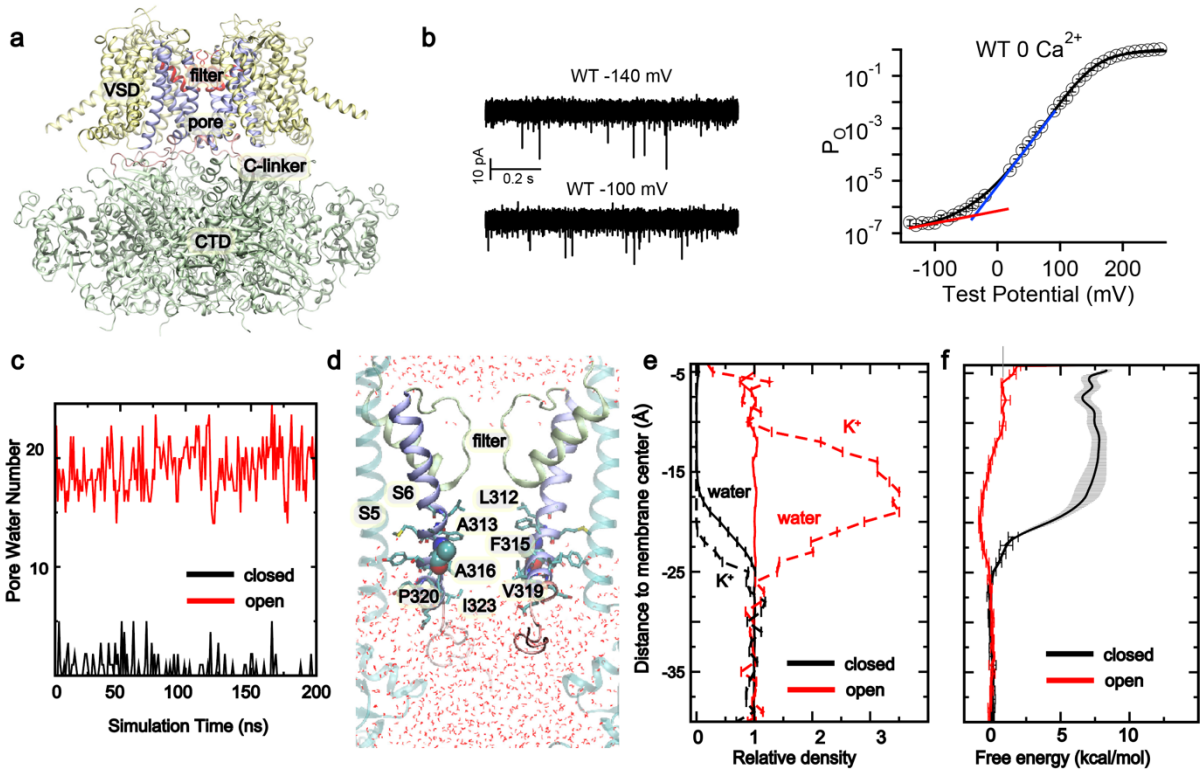

Figure 1. Structure, hydration and ion permeation free energy of BK channels. a) The overall structure of Ca^{2+}-free BK channel (PDB: 6v3g), the C-terminal domain (CTD), C-linker, VSD, pore, and filter are colored in green, pink, yellow, blue and red, respectively. **b)** Representative single-channel currents recorded at -140 mV and -100 mV for the full-length BK channel and the opening probability as a function of membrane voltage. The red and blue slopes illustrate the difference voltage dependence at very negative voltages vs at positive voltages where the channel undergoes the activation transition. **c)** Representative traces showing the number of pore water molecules as a function of time for the Ca^{2+}-free (black) and bound (red) states. **d)** A representative snapshot of the dewetted pore (taken at 100 ns of sim 1, Table S1). Water molecules are represented as wires and the pore-lining residues (L312, A313, F315, V319 and I323) are presented in sticks, and A316 is highlighted with van der Waals spheres. **e**) Average water and K^+ density profiles in the open (red) and closed (black) states, derived directly from the last 150 ns of equilibrium simulations (Table S1, *sim 1* and *2*). **f**) PMFs of K^+ permeation calculated from umbrella sampling for the closed state (black trace, Table S2, *wt0v*), the average K^+ density profile of the open state (red trace, Table S1, *sim 2*). The error bars show the standard deviations from three replicas.

Results

Intrinsic opening of BK channels and leakage of vapor barrier

From the semi-logarithmic plot of open probability (P_o) versus voltage (Fig. 1b), BK channels exhibit two distinct voltage-dependent behaviors. At extremely low voltages, where the voltage sensor typically remains in its resting state, the channels display a small but measurable open probability (around 10^{-6} to 10^{-7}), represented by the red line with a very shallow slope. This phenomenon, known as intrinsic opening, occurs largely independent of voltage sensor activation. In contrast, at mid-range voltages, P_o becomes clearly voltage-dependent, as illustrated by the blue line. BK channels differ significantly from classic potassium channels, such as Shaker channels, in which P_O versus voltage relationship is linear at all voltages (48). To measure the 10^{-7} level of open probability, macroscopic patches containing hundreds or even thousands of channels were used to assess the total open probability (NP_O) at very negative voltages. Calculations revealed that the total opening events last only about 1 millisecond, even over a duration of 10 seconds. Additionally, each opening event is very brief, making it difficult to analyze.

The molecular basis of intrinsic opening of BK channels is poorly understood. Starting from the relaxed cryo-EM structure (Fig. 1a, PDB 6v3g, see Methods), the pore of human BK in the Ca^{2+}-free, closed state readily underwent hydrophobic dewetting transitions during equilibrium atomistic simulations, similar to what was observed previously using different structures (32-34). The closed pore remained stably dewetted throughout subsequent production simulations (*e.g.,* see Fig. 1c). The number of pore waters fluctuated between 0 and up to 5, consistent with a dry pore occupied by water vapor phase (Fig. 1d). The resulting relative density profiles show that there is depletion of water, and consequently K^+, densities from around -15 Å (near P320) to the filter in the closed state pore (Fig. 1e). This dry inner pore region is lined by a series of hydrophobic residues including L312, A313, F315, A316, V319 and P320 (Fig. 1d). The structure of the dry pore is stable during all simulations (Fig. S1) with a diameter of ~7 Å (Fig. S2), physically open and accessible to hydrated ions, channel blockers and various side chain modifying reagents. In contrast, the pore in the Ca^{2+}-bound open channel remained fully solvated throughout the simulations (Fig. 1c), and there is no water or K^+ depletion in the pore (Fig. 1e). Note that the K^+ density peaks at about three times that of the bulk in the open channel, due to the presence of 8 conserved acidic residues near the pore entrance (E321/E324). It has been shown that deleting these charges leads to ~50% drop in the single channel conductance (49).

Interestingly, lipid tails can enter the dewetted pore through the fenestration gap between the

pore lining S6 helices (Fig. S3). This has been observed consistently in previous simulations and likely reflected in densities within the pore in multiple cryo-EM maps (24, 26, 32-34). It is possible that the presence of the lipid tails in the pore help stabilize the dewetted state. During the equilibrium simulations, lipid tails that enter the pore are highly dynamic with average residence time of < 10 ns, which suggests that lipid tails do not show strong preference of nonspecific interactions with the pore wall with respect to the hydrophobic interior of the membrane. Therefore, the presence of lipid tail in the pore is likely a consequence, rather than a driver, of pore dewetting. Indeed, two independent free energy analyses using either the classical force field or a polarizable one have confirmed that lipid presence in the pore is not required for dewetting of the BK pore (34, 50).

We then calculated the potential of mean force (PMF) of K^+ permeation through the pore in both open and closed states. The results show that, while there is no significant free energy barrier for the open (and hydrated) pore, the vapor barrier in the closed (and dry) pore imposes a free energy barrier of $\Delta W \sim 8$ kcal/mol near $z \sim -12$ Å for K^+ to reach the filter from the cytosolic entrance (Fig. 1e, red vs black trace,). As such, even if the channel is driven to 100% in the closed conformational state (e.g., under large negative voltages in absence of intracellular Ca^{2+}), there would be a non-diminishing probability of $P_o \sim e^{-\Delta W/RT} \sim 10^{-6}$ for K^+ to cross the barrier and leak through at room temperature. Strikingly, this estimate is in quantitative agreement with the intrinsic opening probabilities of BK channels (Fig 1b) (6, 51-53). In the classical Horrigan-Cui-Aldrich (HCA) allosteric model of BK activation, the intrinsic opening probability is attributed to some unknown spontaneous activation of the pore when all VSDs are in the resting state (51, 54). Curiously, limiting slope experiments show such spontaneous opening transitions to be extremely brief, typically no longer than 20 μs for the wild type (wt) full-length BK channel (Fig. 1, 2a). The fast transition kinetics is inconsistent with a large-scale pore conformational change such as those involved in voltage-driven opening of BK channels on ms timescales (53). Instead, the fast transient opening is reminiscent of sporadic rehydration dynamics of various hydrophobic nanopores, which readily occurs at tens of ns timescales for carbon nanotubes (55, 56) to ~μs for protein pores with complex shapes and roughed surface (34). Taken together, leakage of the vapor barrier likely explains both the magnitude and kinetics of intrinsic opening of BK channels in limiting slope experiments.

Shallow voltage dependence of intrinsic opening arises mainly from the electric field effects on the permeating K^+

The shallow voltage dependence of intrinsic opening is distinct from the steep dependence driven by VSD activation under depolarizing voltages (51, 54). Its molecular origin is unknown,

even though it presumably arises from the voltage dependence of the putative pore conformational equilibrium with the VSDs at the resting state. To examine if vapor barrier leakage could give rise to the observed voltage dependence, we calculated additional free energy profiles of K^+ permeation at -40, -80, -120 and -160 mV with the backbone heavy atoms of the pore restrained to be the equilibrated conformationally closed state (Table S2; see Methods). The results, summarized in Fig. 2b, show that the free energy barrier of K^+ permeation slightly increases at more negative voltages, from ~8 kcal/mol at 0 mV to ~9.5 kcal/mol at -160 mV. Strikingly, the leakage probabilities estimated from the barrier height are in quantitative agreement with experimental measurements (Fig. 2d, open and filled black circles). Furthermore, the slope estimated from calculated Log(P_o) values from -40 to -160 mV is 0.003 mV^{-1} (Fig 2d, green line), compared to 0.005 mV^{-1} from analysis of the experimental measurement (Fig. 1b). This is an important observation, that a large-scale conformational response of the pore is not required for recapitulating the limiting slope of BK channels.

To determine the origin of the voltage dependence of K^+ permeation free energy barrier, we evaluated the contribution of local electric field. The electric potential along the pore axis was calculated from equilibrium simulations at different voltages with the backbone of the pore restrained (Table S1, *sim 6-10*) (see Methods and Fig. S4). The work to move a K^+ from bulk solvent to the inner pore region against the electric field can be then estimated as $\Delta\Delta W_{(v)} = q\,\Delta E_{(v)}$, where q = +1 for K^+ and $\Delta E_{(v)}$ is the relative eclectic potential with respect to the bulk region. The electric field contribution can be then added to the 0 mV PMF (Fig. 2b, black trace) to directly estimate the voltage dependence of K^+ permeation barrier as $\Delta W^*_{(v)} \sim \Delta W_{(0)} + \Delta\Delta W_{(v)}$, and then the leakage as $P_{o,(V)} \sim e^{-\Delta W^*_{(v)}/RT}$. Remarkably, the resulting leakage probability estimates seem to well reproduce the values derived from the full PMF calculations (Fig. 2d, empty squares vs filled circles). Therefore, the shallow voltage dependence of intrinsic opening of BK channels arises mainly from the effects of the electric field on the permeating K^+ as it enters the inner pore and crosses the vapor barrier.

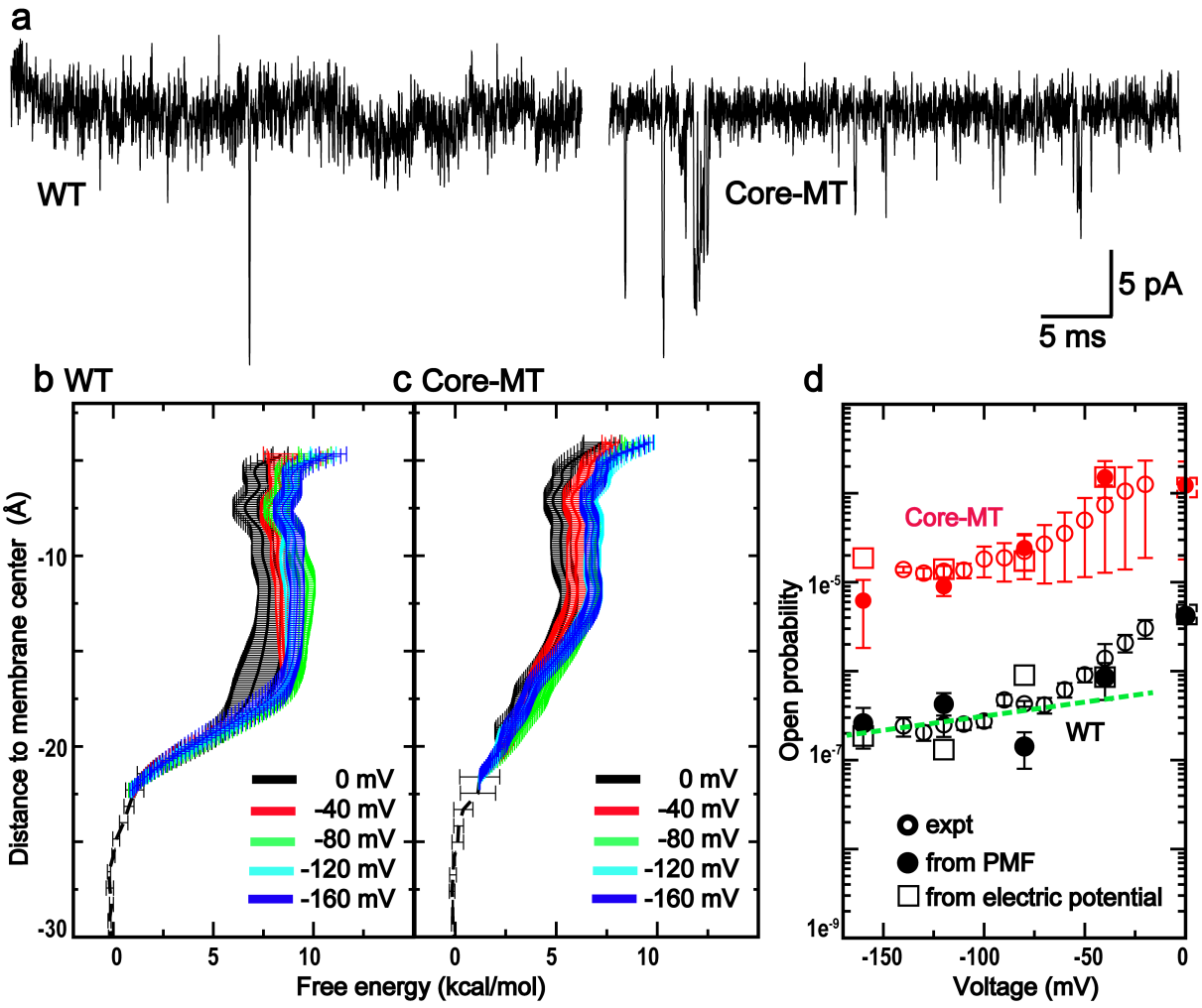

Figure 2. Intrinsic opening of full-length and Core-MT BK channels. a) Representative single-channel currents recorded at -140 mV for the wt (left) and Core-MT (right) BK channels. **b, c)** PMFs of K^+ permeation though the closed pore of the full-length and Core-MT BK channels calculated using umbrella sampling at different voltages (Table S2, sim *wt0mv* to *core-160mv*). **d)** Intrinsic opening probabilities from limiting slope experiments (empty circles), estimated from PMFs in panels b and c (solid circles), and estimated from 0 mV PMFs and electric potential profiles (empty squares). The error bars show the standard deviations from three replicas (simulation) or SEM (experiment). The dashed green line shows the linear fit to opening probabilities calculated at -40 to -160 mV.

Intrinsic opening reports perturbation to the vapor barrier

To further examine if the vapor barrier leakage is indeed the origin of intrinsic opening, we explore two distinct approaches to perturb the inner pore properties and the resulting vapor barrier. The first approach involves the Core-MT construct of BK channels where the whole CTD is removed and replaced by a 11-residue mini-tail from K_V channels (53, 57). Core-MT BK channels is devoid of Ca^{2+} and Mg^{2+} activation but retains voltage-dependent gating. It has been shown that, while the voltage sensor movement (Q-V relationship) of Core-MT only exhibits a small change compared to the full length channel (shifted to left about 20mV), the intrinsic opening probability increases by more than two orders of magnitude (53) (Fig 2d). The equilibrated conformations of the pore are similar in Core-MD and full-length BK channels (Fig. S5). However, the absence of the CTD increases the flexibility of the C-linkers (Fig. 1a), potentially leading to dynamic destabilization of the vapor lock in the closed state. Indeed, free energy calculations reveal that the barrier of K^+ entering the pore is reduced to ~5 kcal/mol at 0 mV (Fig. 2c, black trace), which translates into ~150-fold increase in leakage probability, in excellent agreement with the experiments (Fig. 2d). The voltage dependence of intrinsic opening of Core-MT predicted from the PMFs (Fig. 2c) is also in quantitative agreement with the measured results (Fig. 2d, solid vs empty red circles). Following the same procedure as described above, we further show that the experimentally determined voltage dependence at most negative voltages can be fully explained by the electric field effects and does not require pore conformational response to different membrane voltages (Fig. 2d, red empty squares vs circles).

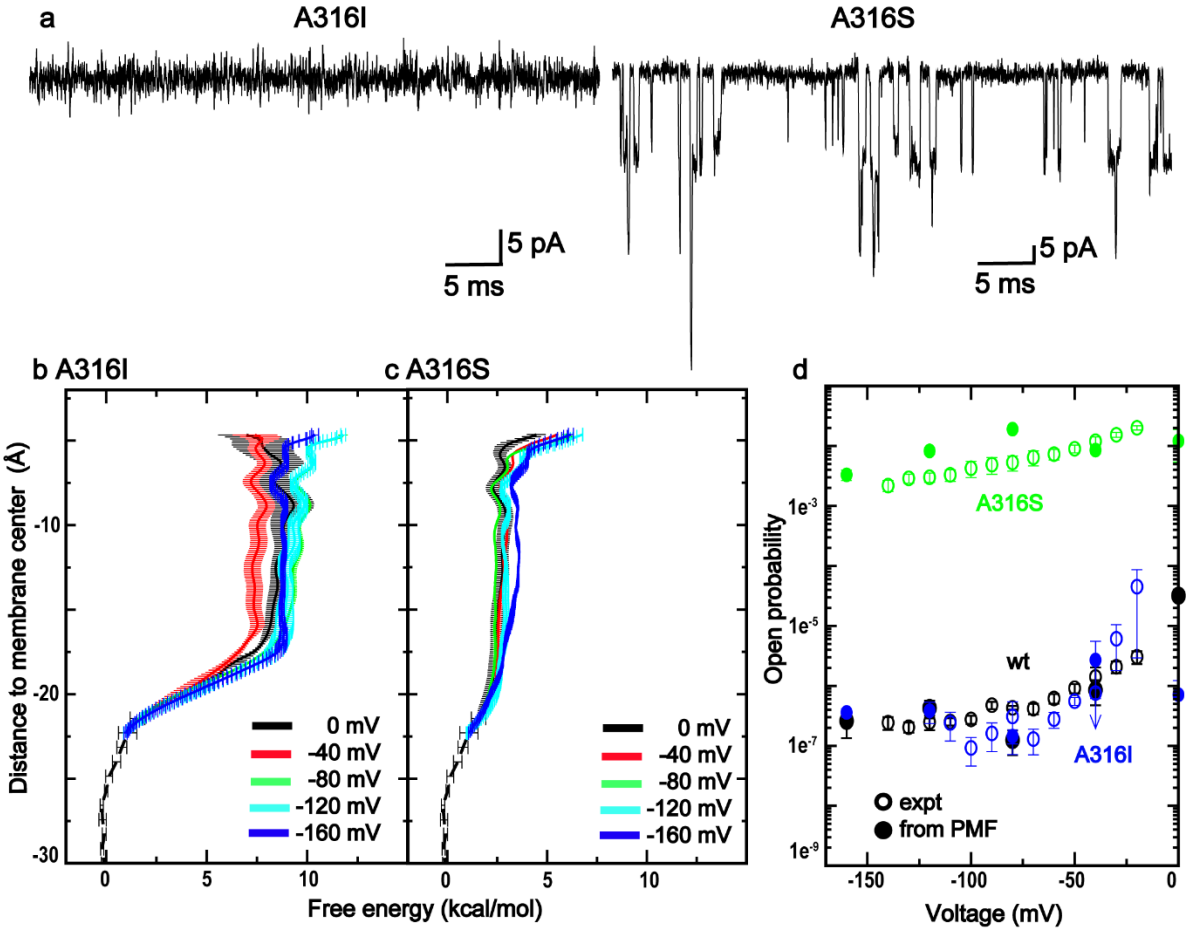

Figure 3. Effects of pore mutations on Intrinsic opening of full-length BK channels. a) Representative single-channel currents recorded for A316I (left) at -100 mV and A316S (right) at -140 mV. **b, c)** PMFs of K^+ permeation though the closed pore of the full-length A316I and A316S mutant BK channels calculated using umbrella sampling at different voltages (Table S2, sim *316I0mv* to *316S-160mv*). **d)** Intrinsic opening probabilities from limiting slope experiments (empty circles) and estimated from PMFs shown in panels b and c (solid circles). The error bars show the standard deviations from three replicas (simulation) or SEM (experiment).

In the second approach, we examined the effects of mutating the pore-lining residues on the vapor barrier and limiting slope measurements. A previous systematic scanning mutagenesis study revealed a strong correlation between the overall hydrophobicity of the pore with gating voltage of BK channels (38). Here we focus on two mutations of A316, located at the center of the vapor barrier. A316I installs a larger hydrophobic sidechain and increase the half activation voltage ($V_{1/2}$) from 163 mV to 353 mV in 0 Ca^{2+}; A316S installs a hydrophilic sidechain and reduces $V_{1/2}$ to 40 mV (38). Equilibrium simulations suggest that these

mutations do not lead to significant changes of the pore conformation itself (Fig. S2). However, alterations of the inner pore hydrophobicity seem to have significant impacts in the vapor barrier. The barrier to K^+ entering the pore is increased to ~ 9 kcal/mol for A316I and decreased to ~ 3 kcal/mol for A316S at 0 mV (Fig. 3b, c). Indeed, the limiting slope measurements show that the intrinsic opening of A316I mutant channel is slightly reduced, even though that it is now at a level near the limit of experimental sensitivity at < -100 mV (Fig. 3d, empty blue circles). F315A exhibits a similar QV and GV relationship at 100 μM Ca^{2+} as A316I. The intrinsic opening probability, calculated from the fitting parameters, was found to be at the 10^{-9} level(58). However, due to measurement limitations, we cannot accurately measure any open probability less than 10^{-8}. This indicates that a patch with 1,000 channels would only experience 0.1 ms opening events over a 10-second duration. In contrast, the intrinsic opening of A316S mutation channel is increased by ~4 orders of magnitude as predicted (Fig. 3, empty green circles). This is also consistent with a previous study of inner pore hydration free energy of BK channels, which shows that A316S destabilizes the dry vapor state by ~4 kcal/mol and A316I stabilizes the vapor phase by ~2 kcal/mol (34). Taken together, both CTD truncation and pore mutations can perturb the stability of the vapor barrier and lead to predictable changes in intrinsic opening that can be measured experimentally.

Discussion

Hydrophobic gating has emerged as a major noncanonical mechanism in ion channels. Specifically for BK channels, which possess a large inner pore with a diameter at minimal of ~nm in the activate state. The ion permeation can be efficiently shut off without complete collapse of the pore to form a physical constriction point. Instead, relatively small conformational changes are required to change the shape and hydrophobicity of the pore such that it can spontaneously dewet to create a vapor barrier during deactivation. In this work, we combine atomistic simulation and electrophysiology to demonstrate that the well-known intrinsic opening of BK channels derives from the leakage vapor barrier, due to a finite free energy barrier it provides for K^+ permeation. We show that vapor barrier leakage quantitatively recapitulates both the magnitude and kinetics of BK intrinsic opening observed experimentally. Our study reveals that the shallow voltage dependence of intrinsic opening at negative voltages does not require conformational response of the pore when VSDs are fully deactivated; instead, it can be readily explained by the effects of local electric field on the permeating K^+ during leakage.

We demonstrate that various mutations can be introduced to affect the dynamics and surface properties of the pore to modulate the stability of vapor barrier in deactivated BK channels. These perturbations lead to predictable changes in the leaking probability and can be validated

directly by measuring intrinsic opening. Therefore, limiting slope experiments provide an experimental essay to study hydrophobic gating for the first time. This essay will enable one to systematically study how hydrophobic gating can be controlled by channel protein properties and binding of various ligands in complex cellular environments. As the intrinsic equilibrium for channel opening is predominantly determined by liquid–vapor equilibrium in the inner pore region, hydrophobic gating can be controlled and regulated solution conditions including the presence of certain metabolites, salt concentration, and external electric field. It is also known that Ca^{2+} binding enhances the intrinsic open probability of BK channels ~10^4-fold at -140 mV (6, 59). Critically, in all Ca^{2+} concentrations the open probability at very negative voltages shows a similar shallow voltage dependence, which is characteristic of vapor barrier leakage but differs from the steep dependence driven by VSD activation at depolarizing voltages. This suggests that Ca^{2+}-dependent activation primarily affects the vapor barrier itself in the closed state. Therefore, intrinsic opening in BK channels may be the fundamental basis for the allosteric mechanism of activation by both voltage and Ca^{2+}.

Methods

Atomistic simulations: initial structures, equilibration, and production runs

The cryo-EM structures of BK channel in the Ca^{2+}-bound (PDB: 6v38) or Ca^{2+}-free (PDB: 6v3g) states (24) were used in all simulations reported in this work. Several short loops missing in one structure were rebuilt using the other structure as template with Swiss-PDB server (e.g. as A567-E576 and N585-E591 is missing in 6v38 but present the 6v3g), as described previously (34). The missing N- and C-terminal segments as well as several long loops (H55-G92, A614-N682, S835-I870) are presumably dynamic and thus not included in the current simulations. Residues before and after the missing segments are capped with either an acetyl group (for N-terminus) or a N-methyl amide (for C-terminus). Standard protonation states under neutral pH were assigned for all titratable residues. We note that PDB 6v3g contains a spurious π-helix turn in residues 317-32 of helix S6, which has not been observed in any other structures of BK channels thus far (22-27) and is unstable in simulations (34). All simulations of the Ca^{2+}-free state reported in this work were thus initiated from a carefully relaxed 6v3g structure from a previous work (34) (see Fig. S1a). The relaxed pore structure was stable during all simulations (e.g., see Fig. S1b).

All initial structures in various states were first inserted in model POPC lipid bilayers and then solvated in TIP3P water using the CHARMM-GUI web server (60). The systems were neutralized and 150 mM KCl added. For full-length BK channel system, the final simulation boxes contain about ~900 lipid molecules (POPC) and ~130,000 water molecules and other

solutes, with a total of ~520,000 atoms and dimensions of ~180 × 180 × 160 $Å^3$. For core-MT system (with CTD removed), the final simulation boxes contain about ~600 lipid molecules (POPC) and ~55,000 water molecules and other solutes, with a total of ~260,000 atoms and dimensions of ~160 × 160 × 100 $Å^3$ The CHARMM36m all-atom force field (61) was used with the CHARMM36 lipid force field (62). All simulations were performed using CUDA-enabled versions of Gromacs 2019 (63, 64). Electrostatic interactions were described by using the Particle Mesh Ewald (PME) algorithm (65) with a cutoff of 12 Å. Van der Waals interactions were cutoff at 12 Å with a smooth switching function starting at 10 Å. Covalent bonds to hydrogen atoms were constrained by the SHAKE algorithm (66), and the MD time step was set at 2 fs. The temperature was maintained at 298 K using the Nose-Hoover thermostat (67, 68). The pressure was maintained semi-isotopically at 1 bar at membrane lateral directions using the Parrinello–Rahman barostat algorithm (69).

All systems were first minimized for 5000 steps using the steepest descent algorithm, followed by a series of equilibration steps where the positions of heavy atoms of the protein and lipid were harmonically restrained (70). Specifically, 6 equilibration step (25 ps for steps 1-3, 100 ps for steps 4-5 and 10 ns for step 6) were performed, where the restrained force constant for proteins were set to 10, 5, 2.5, 1.0, 0.5 and 0.1 $kcal.mol^{-1}.Å^{-2}$, respectively. For lipids, the phosphorus is restrained with force constants of 2.5, 2.5, 1.0 and 0.5, 0.1 and 0.0 $kcal.mol^{-1}.Å^{-2}$, respectively. In the last equilibration step, only protein heavy atoms were harmonically restrained, and the system was equilibrated 10 ns in under NPT (constant particle number, pressure and temperature) conditions.

As summarized in Table S1, three replicas of 200 ns atomistic simulations were first performed for the Ca^{2+}-free and -bound states of WT BK channel (*sim 1* and *2*). In addition, three replicas of simulations were preformed for the core-MT BK channel in the closed state, generated by removing CTD region (residue after R342) from the equilibrated full length BK channel structure (*sim 3*). Two additional equilibrium simulations were performed for the A316I and A316S mutant full-length BK channels in Ca^{2+}-free state (*sim 4* and *5*). The rest of 20 sets of simulations (*sim 6* to *25*) were initiated from various equilibrated structures as noted for various constructs under different membrane voltages to characterize the electric potentials and/or generate relaxed initial structures for subsequent free energy calculations (see below). The external electric field was imposed as described in previous studies (71).

Calculation of K^+ permeation free energy profiles

Umbrella sampling (72) was used to calculate the ion permeation free energy profiles in the closed states under different membrane voltages. To generate initial structures for umbrella

sampling, additional 200 ns simulations with all backbone atoms restrained were performed (-160 mV to 0 mV) for each system (*sim 6-25*, Table S1), to relax the ion, water, lipid, and protein configurations at the voltages imposed. A snapshot was then selected at ~100ns (Table S2), where a single K^+ ion was located near the cytosolic pore entrance (~ 25 Å below the membrane center and ~ 10 Å to E321/E324). The initial conformations for umbrella sampling were then generated by 5-ns steered MD simulations, during which a moving harmonic pulling potential was imposed on the selected K^+ ion with a force constant of 2.0 kcal.mol^{-1}.Å^{-2} (Fig. S1c). Umbrella sampling windows were placed at 2 Å intervals covering z = -6 to -22 Å for the selected K^+. For each window, 3*20 ns simulations were performed (Table S2). A spring force constants of 2.0 kcal.mol^{-1}.Å^{-2} was used to restrain the distance along the membrane normal (*z*) between the ion and membrane center.

Final PMFs were calculated using the weighted histogram analysis method (73). The error bars of the PMF were estimated as standard errors among the three independent sets of free-energy profiles. We note that there is high probability of multiple K^+ occupancy in the hydrated metal-bound pore or ~ -22 Å below the membrane center. The single-ion PMF calculated from umbrella sampling is thus only valid for the dewetted pore region from -6 to -22 Å. The overall PMFs of K^+ permeation for the closed state of channel from -6 to -30 Å were constructed from umbrella sampling and equilibrium MD using linear interpolation at -22 to -24 Å region as done previously (32, 34). The height of free energy barrier is then estimated by the difference between the bulk region (30 to 40 Å below membrane center) and the plateau region in free energy barrier (-15 to -10 Å for full length channel and -12 to -10 Å for Core-MT).

Simulation analysis

Unless stated otherwise, snapshots were extracted every 50 ps after 50 ns of all equilibrium MD trajectories for calculation of statistical distributions. Molecular illustrations were prepared using VMD (74). The ion and water distribution is calculated by MDAnalysis (75). Pore water molecules were identified as those occupying the internal cavity below the selectivity filter, roughly from L312 to the plane defined by the center of mass of P320. Pore profiles are calculated using program HOLE *(76)*. Electric potential maps were calculated using the VMD's PMEPot and VolMap plugins from *sim 6* to *sim 26* (Table S1) (77). The bin size is set to 1 Å during these calculations. To calculate the electric potential profile along pore axis, a cylinder region is selected the center of which is located at the COM filter. The radius is set to 5 Å, which allows the cylinder to cover the internal cavity of the pore without involving protein atoms. The cylinder is then sliced along z axis with 1 Å intervals, the potential of each slice is then estimated as the averages of potential of all bins in this slice.

Mutagenesis and Expression

All mutations studied in this paper were made by using Pfu polymerase (Stratagene) to overlap extension PCR (polymerase chain reaction) from template of the mbr5 splice variant of *mslo1* (Uniprot ID: Q08460) (78). Then the PCR-amplified regions were sequenced to confirm the mutations. mRNA was synthesized in vitro with T3 polymerase (Ambion, Austin, TX) from linearized cDNA. About 0.05–50 or 150–250 ng/oocyte mRNA of the mutations was injected into oocytes (stage IV-V) from female *Xenopus laevis*. After 3-6 days' incubation in 18°C, the oocytes are ready for electrophysiology recordings.

Electrophysiology

All of experimental data were collected from excised inside-out patches on the set-up that was built up by an Axopatch 200-B patch-clamp amplifier (Molecular Devices, Sunnyvale, CA) and ITC-18 interface with Pulse acquisition software (HEKA Electronik, Division of Harvard Bioscience, Holliston, MA). Borosilicate pipettes were pulled using a Sutter P-1000 (Sutter Instrument, Novato, CA) to get 0.5–1.5 MΩ resistance, which were used for inside-out patches from oocyte membrane.

The current signals were obtained with low-pass-filtered at 10 KHz and digitized at 20-μs intervals. Solutions were used in recording: **1)** Pipette solution (in mM): 140 potassium methanesulphonic acid, 20 HEPES, 2 KCl, 2 $MgCl_2$, pH 7.2. **2)** The nominal 0 μM $[Ca^{2+}]_i$ solution (in mM): 140 potassium methanesulphonic acid, 20 HEPES, 2 KCl, 5 EGTA, pH 7.1-7.2. There is about 0.5 nM free $[Ca^{2+}]_i$ in the nominal 0 $[Ca^{2+}]_i$ solution. **3)** 100 μM $[Ca^{2+}]_i$ solution (in mM): 140 potassium methanesulphonic acid, 20 HEPES, 2 KCl, 1 EGTA, and 22 mg/L 18C6TA, 100 μM $[Ca^{2+}]_i$ and pH 7.2.

To measure limiting slope the open probability (P_O), NP_O (total average open probability for all the channels N in a patch) need to be measured first at different negative voltage. Patches containing hundreds or thousands of channels were stimulated with a long pulse (5-10s) at each voltage and the total openings events were obtained by using the integrated currents (area = currents X time) to subtract a baseline, which divided by single channel current and total time to obtain NP_O. The number of the channels in the patches (47, 53, 54) was calculated by $I = N\gamma P_O(V-E_K) = N\,i$, where i means single channel current and $i = \gamma P_O(V-E_K)$.

Acknowledgements

This work is supported by grants R35 GM144045 (J. Chen) and R01 GM149998 (J. Cui).

Author contributions

J. Chen and J. Cui conceived and initiated the studies. Z. Jia and J. Chen performed molecular dynamics simulations and analysis. G. Zhang, J. Shi and J. Cui performed electrophysiological experiments and analyzed data. Z. Jia, G. Zhang, J. Cui and J. Chen wrote the manuscripts, with input from J. Shi.

Competing interests

The authors declare no competing interests.

Data Availability

All relevant simulation/analysis scripts and raw data for the figures can be found on GitHub through: https://github.com/zhiguangjia/BK_vapor_barrier.

Supporting information

The online version contains supplementary material available at https://doi.org/xxxx

References

1. A. Marty, Ca-dependent K channels with large unitary conductance in chromaffin cell membranes. *Nature* **291**, 497-500 (1981).
2. U. S. Lee, J. Cui, BK channel activation: structural and functional insights. *Trends in Neurosciences* **33**, 415-423 (2010).
3. R. MacKinnon, Potassium channels. *FEBS Lett.* **555**, 62-65 (2003).
4. L. Salkoff, A. Butler, G. Ferreira, C. Santi, A. Wei, High-conductance potassium channels of the SLO family. *Nat Rev Neurosci* **7**, 921-931 (2006).
5. H. Yang, G. Zhang, J. Cui, BK channels: multiple sensors, one activation gate. *Frontiers in Physiology* **6** (2015).
6. F. T. Horrigan, R. W. Aldrich, Coupling between Voltage Sensor Activation, Ca^{2+} Binding and Channel Opening in Large Conductance (BK) Potassium Channels. *The Journal of General Physiology* **120**, 267-305 (2002).
7. J. Shi, J. Cui, Intracellular Mg^{2+} Enhances the Function of Bk-Type Ca^{2+}-Activated K^{+} Channels. *The Journal of General Physiology* **118**, 589-606 (2001).
8. K. L. Magleby, Gating mechanism of BK (Slo1) channels: So near, yet so far. *The Journal of General Physiology* **121**, 81-96 (2003).
9. G. F. Contreras *et al.*, A BK (Slo1) channel journey from molecule to physiology. *Channels* **7**, 442-458 (2013).
10. B. H. Bentzen, S.-P. Olesen, L. C. B. Rønn, M. Grunnet, BK channel activators and their therapeutic perspectives. **5** (2014).
11. C. Contet, S. P. Goulding, D. A. Kuljis, A. L. Barth, BK channels in the central nervous system. *International review of neurobiology* **128**, 281-342 (2016).
12. M. A. Zaydman, J. R. Silva, J. Cui, Ion channel associated diseases: overview of molecular mechanisms. *Chem. Rev.* **112**, 6319-6333 (2012).
13. W. Du *et al.*, Calcium-sensitive potassium channelopathy in human epilepsy and paroxysmal movement disorder. *Nature Genetics* **37**, 733-738 (2005).
14. T. Lührs *et al.*, 3D structure of Alzheimer's amyloid-β(1–42) fibrils. *Proceedings of the National Academy of Sciences of the United States of America* **102**, 17342-17347 (2005).
15. R. Brenner *et al.*, BK channel β4 subunit reduces dentate gyrus excitability and protects against temporal lobe seizures. *Nature Neuroscience* **8**, 1752-1759 (2005).
16. M. Sausbier *et al.*, Elevated Blood Pressure Linked to Primary Hyperaldosteronism and Impaired Vasodilation in BK Channel–Deficient Mice. *Circulation* **112**, 60-68 (2005).
17. M. E. Rockman, A. G. Vouga, B. S. Rothberg, Molecular mechanism of BK channel activation by the smooth muscle relaxant NS11021. *Journal of General Physiology* **152** (2020).
18. W. A. Catterall, Ion channel voltage sensors: structure, function, and pathophysiology. *Neuron* **67**, 915-928 (2010).
19. J. Wu *et al.*, Structure of the voltage-gated calcium channel Ca(v)1.1 at 3.6 A resolution. *Nature* **537**, 191-196 (2016).
20. M. J. Lenaeus *et al.*, Structures of closed and open states of a voltage-gated sodium channel. *Proc. Natl. Acad. Sci. U. S. A.* **114**, E3051-E3060 (2017).
21. K. J. Swartz, Towards a structural view of gating in potassium channels. *Nat Rev Neurosci* **5**, 905-916 (2004).
22. R. K. Hite, X. Tao, R. MacKinnon, Structural basis for gating the high-conductance Ca2+-activated K+ channel. *Nature* **541**, 52-57 (2017).
23. X. Tao, R. K. Hite, R. MacKinnon, Cryo-EM structure of the open high-conductance Ca2+-activated K+ channel. *Nature* **541**, 46-51 (2017).
24. X. Tao, R. MacKinnon, Molecular structures of the human Slo1 K(+) channel in complex with beta4. *Elife* **8** (2019).
25. T. Raisch *et al.*, Small molecule modulation of the Drosophila Slo channel elucidated by cryo-EM. *Nat. Commun.* **12**, 7164 (2021).
26. F. C. Gustavo, S. Rong, L. Ramon, P. Eduardo, Structural Basis of Voltage-Dependent Gating in BK Channels and Its Coupling to the Calcium Sensor. *bioRxiv* 10.1101/2023.12.29.573674,

2023.2012.2029.573674 (2023).
27. X. Tao, C. Zhao, R. MacKinnon, Membrane protein isolation and structure determination in cell-derived membrane vesicles. *Proc. Natl. Acad. Sci. U. S. A.* **120**, e2302325120 (2023).
28. J. Cui, BK Channel Gating Mechanisms: Progresses Toward a Better Understanding of Variants Linked Neurological Diseases. *Frontiers in Physiology* **12** (2021).
29. G. Yellen, The voltage-gated potassium channels and their relatives. *Nature* **419**, 35-42 (2002).
30. M. S. P. Sansom *et al.*, Potassium channels: structures, models, simulations. *Biochimica et Biophysica Acta (BBA) - Biomembranes* **1565**, 294-307 (2002).
31. S. B. Long, E. B. Campbell, R. Mackinnon, Crystal structure of a mammalian voltage-dependent Shaker family K+ channel. *Science* **309**, 897-903 (2005).
32. Z. Jia, M. Yazdani, G. Zhang, J. Cui, J. Chen, Hydrophobic gating in BK channels. *Nat. Commun.* **9**, 3408 (2018).
33. R. X. Gu, B. L. de Groot, Central cavity dehydration as a gating mechanism of potassium channels. *Nat. Commun.* **14** (2023).
34. E. B. Nordquist, Z. Jia, J. Chen, Inner pore hydration free energy controls the activation of big potassium channels. *Biophys. J.* **122**, 1158-1167 (2023).
35. W. Li, R. W. Aldrich, Unique inner pore properties of BK channels revealed by quaternary ammonium block. *J. Gen. Physiol.* **124**, 43-57 (2004).
36. C. M. Wilkens, R. W. Aldrich, State-independent block of BK channels by an intracellular quaternary ammonium. *J. Gen. Physiol.* **128**, 347-364 (2006).
37. Y. Zhou, X. M. Xia, C. J. Lingle, Cysteine scanning and modification reveal major differences between BK channels and Kv channels in the inner pore region. *Proc. Natl. Acad. Sci. U. S. A.* **108**, 12161-12166 (2011).
38. X. Chen, J. Yan, R. W. Aldrich, BK channel opening involves side-chain reorientation of multiple deep-pore residues. *Proc. Natl. Acad. Sci. U. S. A.* **111**, E79-88 (2014).
39. M. Yazdani, Z. Jia, J. Chen, Hydrophobic Dewetting in Gating and Regulation of Transmembrane Protein Ion Channels. *J. Chem. Phys.* **153**, 000000 (2020).
40. P. Aryal, M. S. Sansom, S. J. Tucker, Hydrophobic gating in ion channels. *J. Mol. Biol.* **427**, 121-130 (2015).
41. J. Huang, J. Chen, Hydrophobic gating in bundle-crossing ion channels: a case study of TRPV4. *Commun Biol* **6**, 1094 (2023).
42. G. Zhang *et al.*, A charged residue in S4 regulates coupling among the activation gate, voltage, and Ca2+ sensors in BK channels. *The Journal of neuroscience : the official journal of the Society for Neuroscience* **34**, 12280-12288 (2014).
43. D. H. Cox, J. Cui, R. W. Aldrich, Allosteric gating of a large conductance Ca-activated K+ channel. *J. Gen. Physiol.* **110**, 257-281 (1997).
44. J. Cui, D. H. Cox, R. W. Aldrich, Intrinsic voltage dependence and Ca2+ regulation of mslo large conductance Ca-activated K+ channels. *J. Gen. Physiol.* **109**, 647-673 (1997).
45. W. N. Zagotta, T. Hoshi, R. W. Aldrich, Shaker potassium channel gating. III: Evaluation of kinetic models for activation. *Journal of General Physiology* **103**, 321-362 (1994).
46. G. J. Soler-Llavina, M. Holmgren, K. J. Swartz, Defining the conductance of the closed state in a voltage-gated K+ channel. *Neuron* **38**, 61-67 (2003).
47. J. Cui, R. W. Aldrich, Allosteric linkage between voltage and Ca(2+)-dependent activation of BK-type mslo1 K(+) channels. *Biochemistry* **39**, 15612-15619 (2000).
48. L. D. Islas, F. J. Sigworth, Voltage sensitivity and gating charge in Shaker and Shab family potassium channels. *J Gen Physiol* **114**, 723-742 (1999).
49. T. I. Brelidze, X. Niu, K. L. Magleby, A ring of eight conserved negatively charged amino acids doubles the conductance of BK channels and prevents inward rectification. *Proceedings of the National Academy of Sciences* **100**, 9017-9022 (2003).
50. J. Deng, Q. Cui, Electronic Polarization Leads to a Drier Dewetted State for Hydrophobic Gating in the Big Potassium Channel. *The journal of physical chemistry letters* 10.1021/acs.jpclett.4c01359, 7436-7441 (2024).
51. F. T. Horrigan, J. Cui, R. W. Aldrich, Allosteric voltage gating of potassium channels I. Mslo ionic currents in the absence of Ca(2+). *J. Gen. Physiol.* **114**, 277-304 (1999).
52. M. E. Rockman, A. G. Vouga, B. S. Rothberg, Molecular mechanism of BK channel activation

by the smooth muscle relaxant NS11021. *J. Gen. Physiol.* **152** (2020).
53. G. Zhang *et al.*, Deletion of cytosolic gating ring decreases gate and voltage sensor coupling in BK channels. *J. Gen. Physiol.* **149**, 373-387 (2017).
54. F. T. Horrigan, R. W. Aldrich, Allosteric voltage gating of potassium channels II. Mslo channel gating charge movement in the absence of Ca(2+). *J. Gen. Physiol.* **114**, 305-336 (1999).
55. J. C. Rasaiah, S. Garde, G. Hummer, Water in nonpolar confinement: From nanotubes to proteins and beyond. *Annu. Rev. Phys. Chem.* **59**, 713-740 (2008).
56. G. Klesse, S. J. Tucker, M. S. P. Sansom, Electric Field Induced Wetting of a Hydrophobic Gate in a Model Nanopore Based on the 5-HT3 Receptor Channel. *ACS Nano* **14**, 10480-10491 (2020).
57. G. Budelli, Y. Y. Geng, A. Butler, K. L. Magleby, L. Salkoff, Properties of Slo1 K+ channels with and without the gating ring. *Proc. Natl. Acad. Sci. U. S. A.* **110**, 16657-16662 (2013).
58. W. Carrasquel-Ursulaez *et al.*, Hydrophobic interaction between contiguous residues in the S6 transmembrane segment acts as a stimuli integration node in the BK channel. *Journal of General Physiology* **145**, 61-74 (2014).
59. J. Yang *et al.*, An epilepsy/dyskinesia-associated mutation enhances BK channel activation by potentiating Ca2+ sensing. *Neuron* **66**, 871-883 (2010).
60. J. Lee *et al.*, CHARMM-GUI input generator for NAMD, GROMACS, AMBER, OpenMM, and CHARMM/OpenMM simulations using the CHARMM36 additive force field. *J. Chem. Theory Comput.* **12**, 405-413 (2016).
61. J. Huang *et al.*, CHARMM36m: an improved force field for folded and intrinsically disordered proteins. *Nature Methods* **14**, 71 (2016).
62. J. B. Klauda *et al.*, Update of the CHARMM all-atom additive force field for lipids: Validation on six lipid types. *The Journal of Physical Chemistry B* **114**, 7830-7843 (2010).
63. B. Hess, C. Kutzner, D. van der Spoel, E. Lindahl, GROMACS 4: algorithms for highly efficient, load-balanced, and scalable molecular simulation. *J. Chem. Theory Comput.* **4**, 435-447 (2008).
64. M. J. Abraham *et al.*, GROMACS: High performance molecular simulations through multi-level parallelism from laptops to supercomputers. *SoftwareX* **1–2**, 19-25 (2015).
65. T. Darden, D. York, L. Pedersen, Particle mesh Ewald: An *N*-log (*N*) method for Ewald sums in large systems. *The Journal of Chemical Physics* **98**, 10089 (1993).
66. J.-P. Ryckaert, G. Ciccotti, H. J. C. Berendsen, Numerical integration of the cartesian equations of motion of a system with constraints: molecular dynamics of n-alkanes. *J. Comput. Phys.* **23**, 327-341 (1977).
67. S. Nosé, A unified formulation of the constant temperature molecular dynamics methods. *The Journal of Chemical Physics* **81**, 511-519 (1984).
68. W. G. Hoover, Canonical dynamics: Equilibrium phase-space distributions. *Phys. Rev. A* **31**, 1695-1697 (1985).
69. M. Parrinello, A. Rahman, Polymorphic transitions in single crystals: A new molecular dynamics method. *J. Appl. Phys.* **52**, 7182-7190 (1981).
70. S. Jo, T. Kim, W. Im, Automated Builder and Database of Protein/Membrane Complexes for Molecular Dynamics Simulations. *PLoS One* **2**, e880 (2007).
71. J. Gumbart, F. Khalili-Araghi, M. Sotomayor, B. Roux, Constant electric field simulations of the membrane potential illustrated with simple systems. *Biochimica et Biophysica Acta (BBA) - Biomembranes* **1818**, 294-302 (2012).
72. G. M. Torrie, J. P. Valleau, Non-Physical Sampling Distributions in Monte-Carlo Free-Energy Estimation - Umbrella Sampling. *J. Comput. Phys.* **23**, 187-199 (1977).
73. S. Kumar, D. Bouzida, R. H. Swendsen, P. A. Kollman, J. M. Rosenberg, The Weighted Histogram Analysis Method for Free-Energy Calculations on Biomolecules .1. the Method. *J. Comput. Chem.* **13**, 1011-1021 (1992).
74. W. Humphrey, A. Dalke, K. Schulten, VMD: Visual molecular dynamics. *J. Mol. Graph.* **14**, 33-& (1996).
75. N. Michaud-Agrawal, E. J. Denning, T. B. Woolf, O. Beckstein, MDAnalysis: A toolkit for the analysis of molecular dynamics simulations. *J. Comput. Chem.* **32**, 2319-2327 (2011).
76. O. S. Smart, J. G. Neduvelil, X. Wang, B. A. Wallace, M. S. P. Sansom, HOLE: A program for

the analysis of the pore dimensions of ion channel structural models. *J. Mol. Graphics Modell.* **14**, 354-& (1996).

77. A. Aksimentiev, K. Schulten, Imaging alpha-hemolysin with molecular dynamics: ionic conductance, osmotic permeability, and the electrostatic potential map. *Biophys. J.* **88**, 3745-3761 (2005).
78. A. Butler, S. Tsunoda, D. P. McCobb, A. Wei, L. Salkoff, mSlo, a complex mouse gene encoding "maxi" calcium-activated potassium channels. *Science* **261**, 221-224 (1993).

Supplementary Tables

Table S1. Summary of equilibrium atomistic simulations

Systems	Initial Structure	Restraint	State	Voltage (mV)	Mutation	Length (ns)
sim 1	Relaxed 6v3g	backbone of filter and CTD[1]	closed	0	wt	200 * 3
sim 2	6v38 w/ Mg^{2+}/Ca^{2+}	backbone of filter and CTD	open	0	wt	200 * 3
sim 3	Relaxed 6v3g	backbone of filter and C-linker terminus	closed	0	Core-MT	200 * 3
sim 4	Relaxed 6v3g	backbone of filter and CTD	closed	0	A316I	200
sim 5	Relaxed 6v3g	backbone of filter and CTD[2]	closed	0	A316S	200
sim 6	100 ns, sim1	all backbone	closed	0	wt	200 * 3
sim 7	100 ns, sim1	all backbone	closed	-40	wt	200 * 3
sim 8	100 ns, sim1	all backbone	closed	-80	wt	200 * 3
sim 9	100 ns, sim1	all backbone	closed	-120	wt	200 * 3
sim 10	100 ns, sim1	all backbone	closed	-160	wt	200 * 3
sim 11	200 ns, sim3	all backbone	closed	0	Core-MT	200 * 3
sim 12	200 ns, sim3	all backbone	closed	-40	Core-MT	200 * 3
sim 13	200 ns, sim3	all backbone	closed	-80	Core-MT	200 * 3
sim 14	200 ns, sim3	all backbone	closed	-120	Core-MT	200 * 3
sim 15	200 ns, sim3	all backbone	closed	-160	Core-MT	200 * 3
sim 16	200 ns, sim4	all backbone	closed	0	A316I	200
sim 17	200 ns, sim4	all backbone	closed	-40	A316I	200
sim 18	200 ns, sim4	all backbone	closed	-80	A316I	200
sim 19	200 ns, sim4	all backbone	closed	-120	A316I	200
sim 20	200 ns, sim4	all backbone	closed	-160	A316I	200
sim 21	200 ns, sim5	all backbone	closed	0	A316S	200
sim 22	200 ns, sim5	all backbone	closed	-40	A316S	200
sim 23	200 ns, sim5	all backbone	closed	-80	A316S	200
sim 24	200 ns, sim5	all backbone	closed	-120	A316S	200
sim 25	200 ns, sim5	all backbone	closed	-160	A316S	200

[1]The P-loop/filter (T273 to D292) and RCK2 (A614 to C-terminus) are positionally restrained with a harmonic force constant of 0.5 $kcal.mol^{-1}.Å^{-2}$

[2]The P-loop/filter (T273 to D292) and C- are positionally restrained with a harmonic force constants of 0.5 $kcal.mol^{-1}.Å^{-2}$

Table S2. Summary of umbrella sampling simulations

System	Initial Structure	Voltage (mV)	Mutations/Ligands	Length
wt0mv	100 ns, sim6	0	wt	9 window * 3 replies * 20 ns
wt-40mv	100 ns, sim7	-40	wt	9 window * 3 replies * 20 ns
wt-80mv	100 ns, sim8	-80	wt	9 window * 3 replies * 20 ns
wt-120mv	100 ns, sim9	-120	wt	9 window * 3 replies * 20 ns
wt-160mv	100 ns, sim10	-160	wt	9 window * 3 replies * 20 ns
core0mv	100 ns, sim11	0	Core-MT	9 window * 3 replies * 20 ns
core-40mv	100 ns, sim12	-40	Core-MT	9 window * 3 replies * 20 ns
core-80mv	100 ns, sim13	-80	Core-MT	9 window * 3 replies * 20 ns
core-120mv	100 ns, sim14	-120	Core-MT	9 window * 3 replies * 20 ns
core-160mv	100 ns, sim15	-160	Core-MT	9 window * 3 replies * 20 ns
316I0mv	100 ns, sim16	0	A316I	9 window * 3 replies * 20 ns
316I-40mv	100 ns, sim17	-40	A316I	9 window * 3 replies * 20 ns
316I-80mv	100 ns, sim18	-80	A316I	9 window * 3 replies * 20 ns
316I-120mv	100 ns, sim19	-120	A316I	9 window * 3 replies * 20 ns
316I-160mv	100 ns, sim20	-160	A316I	9 window * 3 replies * 20 ns
316S0mv	100 ns, sim21	0	A316S	9 window * 3 replies * 20 ns
316S-40mv	100 ns, sim22	-40	A316S	9 window * 3 replies * 20 ns
316S-80mv	100 ns, sim23	-80	A316S	9 window * 3 replies * 20 ns
316S-120mv	100 ns, sim24	-120	A316S	9 window * 3 replies * 20 ns
316S-160mv	100 ns, sim25	-160	A316S	9 window * 3 replies * 20 ns

Supplementary Figures

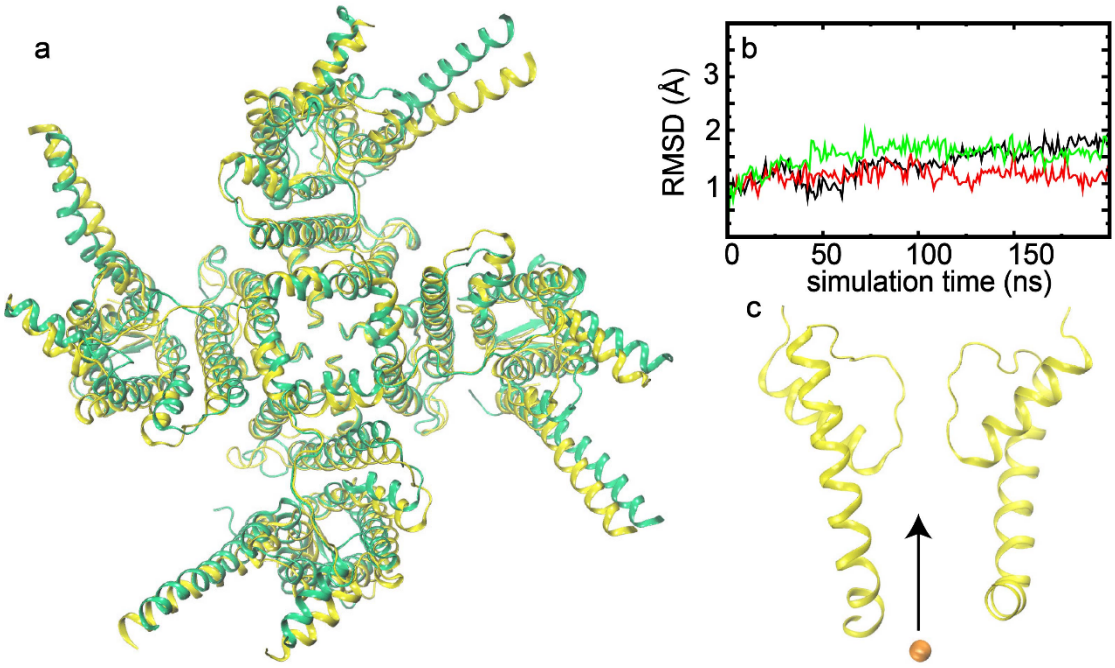

Figure S1. a) Superposition of the transmembrane domain of equilibrated wt BK (green cartoon) and the original cryo-EM structure (PDB: 6v3g, yellow cartoon). **b)** Backbone RMSD of the pore region (F307 to L325) with respect to the initial structure during three replicas of *sim 1* (Table S1). **c)** Schematic illustration of pulling a K^+ ion into the pore to generate initial configurations for umbrella sampling. The arrow indicates the pulling direction.

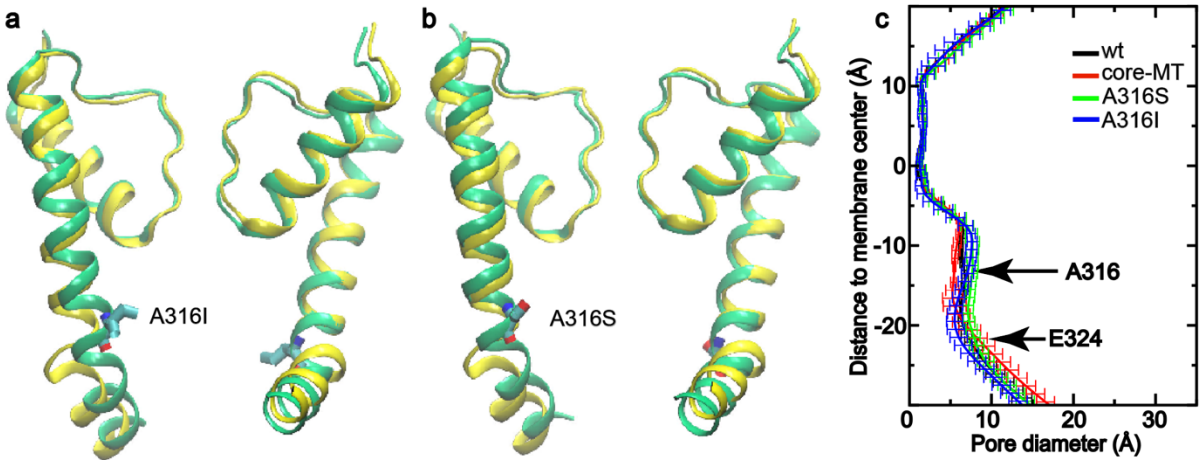

Figure S2. a-b) Superposition of the equilibrated pore mutant channels (200 ns, *sim 4* and *5*, green cartoon) and the original cryo-EM structure (PDB: 6v3g, yellow cartoon); **c)** Pore profiles derived from the last 150 ns of equilibration simulations of wt (black, *sim 1*), core-MT (red, *sim 3*), and pore mutant channels (blue: A316I, and green: A316S; *sim 4* and *5*).

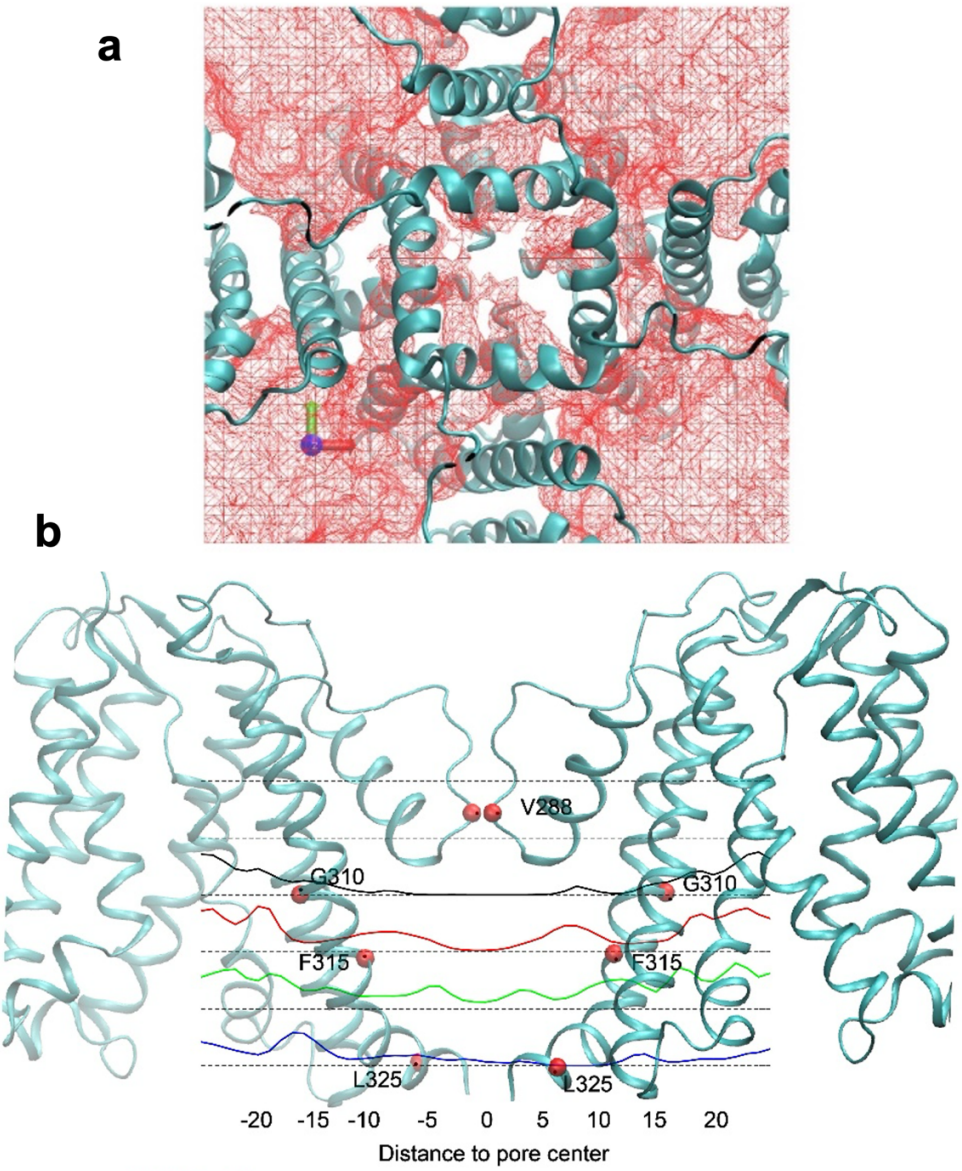

Figure S3. a) Density of lipid tails near the pore of wt BK in the Ca^{2+}-free state, calculated using the last 150 ns of equilibrium simulations (Table S1, *sim 1*). The density is plotted as red mesh with a cutoff of 0.03 atom/Å3. **b)** Distribution of lipid tails at various z-positions along the central axis of the pore. The mean lifetime of lipid tails in the pore is < 10 ns.

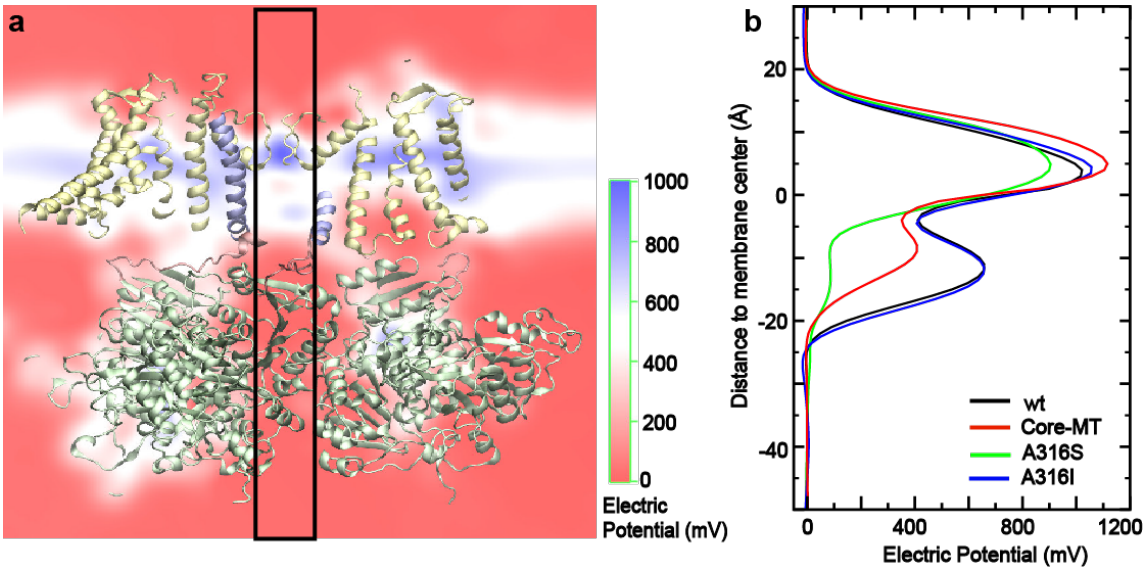

Figure S4. a) Time-averaged electric potential (from *sim 1*) on a slice crosses the center of the pore for illustration. The region used to calculate the electric potential profile is labeled as a black rectangle. **b)** The electric potential profiles at 0 mV for various BK constructs.

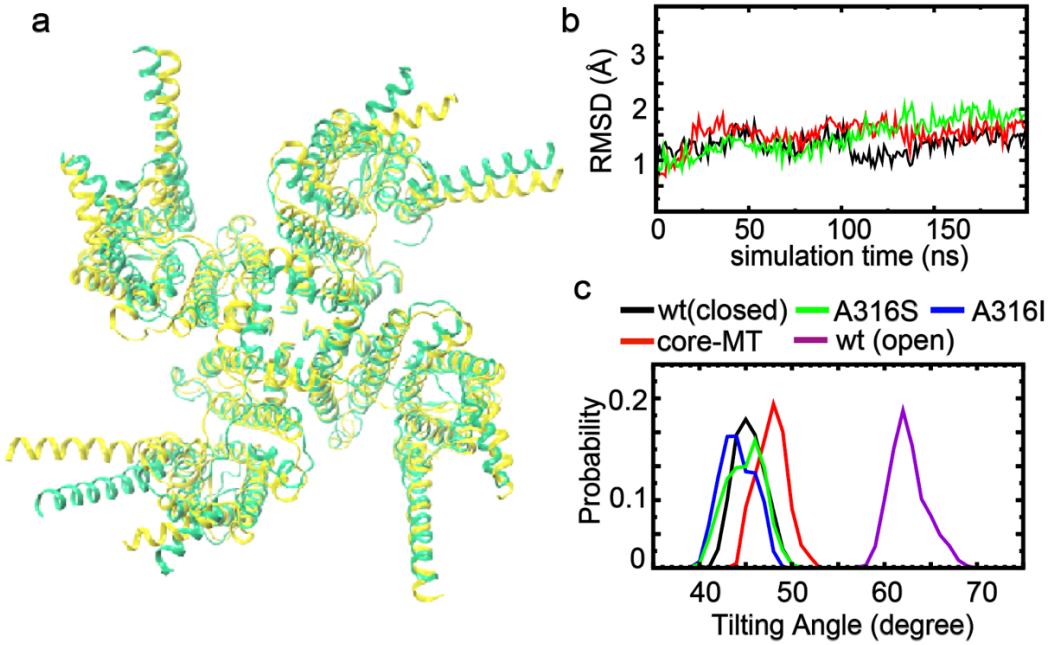

Figure S5. a) Superposition of the transmembrane domain of equilibrated Core-MT BK (green cartoon) and cryo-EM structure (PDB: 6v3g, yellow cartoon). **b)** Backbone RMSD of the pore region (F307 to L325) with respect to initial structure during the three replicas of core-MT ; **c)** Distribution of pore helix (S6, 313-325) tilting angle from simulations of the full length BK channel Ca^{2+}-free state (black, sim 1), Core-MT (red, sim 3) mutated (red (316I) and green (A316S), sim 4 and 5) and full length Ca^{2+}-bound BK channel (purple, sim 2).